

1 Probabilistic cell/domain-type assignment of spatial 2 transcriptomics data with SpatialAnno

3 Xingjie Shi^{1,†,*}, Yi Yang^{2,†}, Xiaohui Ma³, Yong Zhou¹, Zhenxing Guo⁴,
4 Chaolong Wang⁵, Jin Liu^{2,*}

5 ¹KLATASDS-MOE, Academy of Statistics and Interdisciplinary Sciences,
6 School of Statistics, East China Normal University

7 ²Centre for Quantitative Medicine, Health Services & Systems Research,
8 Duke-NUS Medical School

9 ³College for Mathematics and Statistics, South-Central Minzu University

10 ⁴School of Data Science, The Chinese University of Hong Kong, Shenzhen

11 ⁵ Department of Epidemiology and Biostatistics, School of Public Health,
12 Tongji Medical College, Huazhong University of Science and Technology

13 Abstract

14 In the analysis of both single-cell RNA sequencing (scRNA-seq) and spatially resolved
15 transcriptomics (SRT) data, classifying cells/spots into cell/domain types is an essential
16 analytic step for many secondary analyses. Most of the existing annotation methods have
17 been developed for scRNA-seq datasets without any consideration of spatial information.
18 Here, we present SpatialAnno, an efficient and accurate annotation method for spatial
19 transcriptomics datasets, with the capability to effectively leverage a large number of
20 non-marker genes as well as “qualitative” information about marker genes without using
21 a reference dataset. Uniquely, SpatialAnno estimates low-dimensional embeddings for a
22 large number of non-marker genes via a factor model while promoting spatial smoothness
23 among neighboring spots via a Potts model. Using both simulated and four real spatial
24 transcriptomics datasets from the 10x Visium, ST, Slide-seqV1/2, and seqFISH platforms,
25 we showcase the method’s improved spatial annotation accuracy, including its robustness
26 to the inclusion of marker genes for irrelevant cell/domain types and to various degrees of
27 marker gene misspecification. SpatialAnno is computationally scalable and applicable
28 to SRT datasets from different platforms. Furthermore, the estimated embeddings for
29 cellular biological effects facilitate many downstream analyses.

*Corresponding author, xjshi@fem.ecnu.edu.cn, jin.liu@duke-nus.edu.sg.

† The first two authors have contributed equally to this work.

30 Introduction

31 With the rapid advancement of spatially resolved transcriptomics (SRT) technologies, it has
32 become feasible to comprehensively characterize the gene expression profiles of tissues while
33 retaining information on their physical locations. Among the already developed SRT methods,
34 *in situ* hybridization (ISH) technologies, such as MERFISH¹ and seqFISH², provide single-
35 molecule resolution for targeted genes but require prior knowledge of the genes of interest;
36 while *in situ* capturing technologies, such as 10x Visium, Slide-seqV1/2³, and Stereo-seq⁴,
37 are unbiased and provide transcriptome-wide expression measurements. Among the *in situ*
38 capturing technologies, there has been a dramatic improvement in spatial resolution, with
39 spot sizes ranging from 55 μm in 10x Visium, 10 μm in Slide-seqV2, to $<1 \mu\text{m}$ in Stereo-seq.
40 These SRT technologies provide an opportunity to study how the spatial organization of gene
41 expression in tissues relates to tissue functions⁵. To characterize the transcriptomic landscape
42 within a spatial context, assigning cell/domain types in relation to tissue location is an essential
43 analytic step that provides comprehensive spatially resolved maps of tissue heterogeneity⁶.

44 Conventionally, spatial annotation relies on the manual assignment of cell/domain clusters
45 using known marker genes that are readily available from existing studies or databases^{7,8}. A
46 general workflow begins with the unsupervised clustering of spots based on their transcriptomic
47 profiles; this is followed by an examination of the differentially expressed genes (DEGs) specific
48 to each cluster; and finally, the DEGs are manually matched with known marker genes to assign
49 cell/domain types to spatial spots. This type of workflow requires sufficient knowledge of the
50 biology and markers of the cell/domain types, but it can be time-consuming, labor-intensive,
51 and less reproducible^{6,9}. Moreover, these workflows are sensitive to the choice of clustering
52 methods, presenting challenges in the downstream interpretations¹⁰. An improved strategy for
53 spatial annotation is to automatically annotate the identified clusters using either reference
54 data or leveraging existing information on the cell/domain types. Performing annotations with
55 reference data has been shown to be successful in the context of single-cell RNA sequencing
56 (scRNA-seq) analysis. For example, scmap performs cell annotation by projecting existing
57 reference data with known cell types onto cells in the study data¹¹. However, the success of
58 this type of analysis relies on the availability of reference data that are “similar” to the study
59 data. On the other hand, the availability of data on cell-type-specific marker genes from existing
60 studies or databases, potentially obtained using either low-throughput or high-throughput
61 systems, further necessitates the efficient utilization of marker-gene information in a “qualitative”
62 manner. To this end, a number of methods have been developed for scRNA-seq data without
63 any consideration of spatial information, including SCINA¹², Garnett¹³, CellAssign¹⁴, and
64 scSorter¹⁵.

65 To efficiently utilize the existing knowledge base on marker genes for cell/domain types, an
66 ideal annotation method for SRT datasets should be capable of leveraging this “qualitative”
67 information on marker genes with data on non-marker genes while incorporating spatial
68 information to promote spatial smoothness in the cell/domain-type annotation. Because the
69 proportion of non-marker genes is much larger than that of marker genes, non-marker genes also
70 harbor substantial amounts of biological information that can be used to separate cell/domain
71 types. Annotation methods capable of leveraging marker with non-marker genes can improve
72 our ability to detect spatial cell/domain clusters^{14,15}. However, the high-dimensional nature of

73 non-marker genes makes the annotation task more challenging and, moreover, requires proper
74 and efficient modeling of this information. Furthermore, for SRT datasets, especially those
75 from tissue sections with laminar structures, e.g., brain regions, a desirable spatial annotation
76 method would additionally be able to leverage spatial information.

77 To address the challenges presented by spatial annotation, we propose the use of a proba-
78 bilistic model, SpatialAnno, which performs cell/domain-type assignments for SRT data and
79 has the capability of leveraging non-marker genes to assign cell/domain types via a factor
80 model while accounting for spatial information via a Potts model^{16,17}. To effectively leverage
81 a large number of non-marker genes and overcome the curse of dimensionality, SpatialAnno
82 uniquely models expression levels in a factor model governed by separable cell/domain-type low-
83 dimensional embeddings. As a result, SpatialAnno not only performs spatial cell/domain-type
84 assignments with better accuracy, but also estimates cell/domain-type-aware embeddings that
85 can facilitate downstream analyses. We illustrate the benefits of SpatialAnno through extensive
86 simulations and analyses of a diverse range of example datasets collated using different spatial
87 transcriptomics technologies. To show the improved spatial annotation accuracy, we applied
88 SpatialAnno to analyze a 10x Visium datasets for 12 human dorsolateral prefrontal cortex
89 (DLPFC) samples. To illustrate the effectiveness of SpatialAnno in leveraging non-marker
90 genes, we analyzed a mouse olfactory bulb (OB) dataset generated using the ST technology.
91 Using Slide-seqV1/2 datasets for the mouse hippocampus, we demonstrated that SpatialAnno
92 can correctly identify cell-type distribution at near-cell resolution. The utility of SpatialAnno
93 to estimate low-dimensional embeddings is demonstrated by a seqFISH dataset for the mouse
94 embryo.

95 Results

96 Overview of SpatialAnno

97 Similarly to other methods that assign known cell/domain types to cells using information about
98 marker genes, SpatialAnno takes as input normalized gene expression matrix, spatial location
99 information, and a list of marker genes for known cell/domain types (Fig. 1a). SpatialAnno
100 automatically performs cell/domain-type assignments while providing low-dimensional embed-
101 dings for all spatial spots. Based on the latent cell/domain type for each spot, SpatialAnno
102 builds a “semi-supervised” Gaussian mixture model to modulate the over-expression of marker
103 genes and a hierarchical factor model to relate non-marker gene expression to the cell/domain
104 separable latent embeddings while accounting for the spatial smoothness of the cell/domain
105 types with a Potts model (Fig. 1b). Uniquely, SpatialAnno, via the factor model, allows for
106 the assignment of cell/domain types that leverage a large number of non-marker genes, and,
107 via the Potts model, is more likely to assign the same cell/domain type to neighboring spots,
108 promoting spatial smoothness in the cell/domain types. Notably, with expression data for both
109 marker and non-marker genes, SpatialAnno simultaneously assigns each spot known cell/domain
110 types while obtaining low-dimensional embeddings for each spot, which can facilitate other
111 downstream analyses. Similarly to other methods, SpatialAnno automatically labels spatial
112 spots that do not belong to any known cell/domain type as “unknown”, preventing incorrect
113 assignment when novel cell/domain types are present.

114 Validation using simulated data

115 We conducted simulations to evaluate the performance of SpatialAnno and compared the results
116 with those of non-spatial annotation methods commonly applied to scRNA-seq data: SCINA,
117 Garnett, CellAssign, and scSorter (see Methods). The simulation details are provided in the
118 Methods section. Briefly, we simulated gene expression counts using a splatter model¹⁸ for
119 seven cortical layers using labels from the DLPFC data. Then, we selected five marker genes for
120 each layer based on the log-fold change in expression (see Methods). In total, we obtained 35
121 marker genes and 2000 non-marker genes for 3639 spots from seven layers. For each simulated
122 SRT dataset, we applied SpatialAnno and the four other methods to perform spatial domain
123 annotation. We used Cohen's Kappa, mean F1 (mF1) score, and classification accuracy (ACC)
124 (see Methods) to quantify the concordance between the detected spatial domains and the seven
125 labeled cortical layers^{11,14}. We performed 50 replicate simulations for each setting.

126 When the correct number of layers was specified, SpatialAnno (Kappa=0.903, mF1=0.807,
127 and ACC = 0.922) outperformed all other methods in terms of annotation accuracy (Fig. 1c;
128 number of cell/domain types = 7). After varying the number of cell/domain types with marker
129 genes, the SpatialAnno annotation still outperformed all other methods (Fig. 1c; number of
130 cell/domain types = 5 or 9). Unsurprisingly, SpatialAnno performed worse when there were
131 five cell/domain types with marker genes (Kappa=0.839, mF1=0.729, and ACC = 0.883)
132 than seven or nine (Kappa=0.900, mF1=0.803, and ACC = 0.918). The latter two cases
133 (seven and nine cell/domain types) led to comparable annotation performances for SpatialAnno
134 and CellAssign. In contrast, annotation performance decreased for the other methods when
135 we included marker genes for irrelevant cell/domain types. We examined the robustness of
136 SpatialAnno when there were various degrees of marker gene misspecification (Fig. 1d). As
137 the proportion of misspecified marker genes increased, the annotation performance decreased
138 for all methods, but SpatialAnno still outperformed all other methods in terms of annotation
139 accuracy (Kappa, mF1, and ACC).

140 Next, we examined the effectiveness of SpatialAnno, which leverages various amounts of
141 non-marker information compared with the scSorter and Garnett methods, also capable of
142 leveraging non-marker genes (Supplementary Fig. 1a). As the number of non-marker genes
143 increased from 60 to 2000, SpatialAnno showed 10.3%, 21.9% and 8.1% improvements in
144 annotation accuracy for Kappa, mF1 and ACC, respectively, while the annotation accuracies
145 of scSorter and Garnett were almost unchanged, with the changes being -0.6% and -0.6% for
146 Kappa, 1.7% and -0.1% for mF1, and -0.1% and -0.7% for ACC, respectively. These results
147 suggest that SpatialAnno can effectively leverage various numbers of non-marker genes.

148 In addition to the spatial spots being accurately annotated, the low-dimensional embed-
149 ding of non-marker genes from SpatialAnno was cell/domain-type informative. Clustering
150 performance using low-dimensional embeddings with either marker genes or non-marker genes,
151 or a combination of the two, with a comparable adjusted rand index (ARI) between marker
152 and non-marker genes, is shown in Supplementary Fig. 1b & c. Not surprisingly, combining
153 both embeddings for marker and non-marker genes led to improved ARIs in all scenarios,
154 demonstrating the benefits of borrowing information from non-marker genes when annotating
155 cell/domain types. In addition, the Pearson's correlation coefficients for the relationship between
156 the observed expression and the estimated labels, given the embeddings from SpatialAnno,

157 were much smaller than those for the principal component analysis (PCA), but comparable
158 to those for the DR-SC¹⁹ (Supplementary Fig. 1d & e). These results suggest SpatialAnno
159 embeddings can capture cell/domain-type-relevant information for each spot, thus facilitating
160 the downstream analysis.

161 Finally, we evaluated the computational efficiency of all methods for different numbers
162 of cell/domain types, as shown in Supplementary Fig. 1f. SpatialAnno was computationally
163 efficient and comparable in efficiency to SCINA and scSorter, and all three were faster than
164 Garnett and CellAssign.

165 **SpatialAnno improves annotations of known layers in human dorso- 166 lateral prefrontal cortex**

167 We applied SpatialAnno and the four methods to the analysis of human dorsolateral prefrontal
168 cortex (DLPFC) 10x Visium data²⁰. In this dataset, there were 12 tissue sections from three
169 adult donors with a median depth of 291 million reads for each sample, a median of 3844
170 spatial spots per section, and a mean of 33,538 genes per spot (Supplementary Table 1). Each
171 tissue section was manually annotated to a DLPFC layer and white matter (WM) based on
172 the cytoarchitecture²⁰. Taking sample ID151507 as a reference, we constructed a marker-gene
173 list that contained five marker genes for each of the seven layers (see Methods).

174 Taking manual annotations as ground truth, we first evaluated the performance of spatial
175 annotation using Kappa, mF1, and ACC for each of the 12 tissue sections (Fig. 2a). SpatialAnno
176 annotated spatial domains more accurately (median Kappa=0.524, median mF1=0.494, and
177 median ACC=0.628) than scSorter (median Kappa=0.381, median mF1=0.366, and median
178 ACC=0.489), SCINA (median Kappa=0.209, median mF1=0.337, and median ACC=0.307),
179 Garnett (median Kappa=0.24, median mF1=0.32, and median ACC=0.339), and CellAssign
180 (median Kappa=0.253, median mF1=0.29 and median ACC=0.326). The heatmap of the
181 spatial assignments from SpatialAnno and the other methods and the manual annotations for
182 sample ID151673 are shown in Fig. 2b. SpatialAnno achieved the best annotation accuracy
183 (Kappa=0.634, mF1=0.619, and ACC=0.685), while the annotations from scSorter, SCINA,
184 and CellAssign were only accurate for the WM, and Garnett completely failed to assign the
185 WM region. Notably, the domains identified in SpatialAnno were spatially smooth, continuous,
186 and well matched with the elevated expression levels of marker genes for each layer (Fig. 2c
187 and Supplementary Fig. 2-13), such as *Pcp4* and *Mobp* that are marker genes for layer 5 and
188 WM, respectively^{20,21}.

189 To evaluate the robustness of SpatialAnno, we obtained marker genes from the other DLPFC
190 tissue section that contained seven layers and performed spatial annotation for the remainder
191 of the 11 tissue sections (see Methods). Using the top 5/10/15 DEGs as marker genes for each
192 layer, SpatialAnno achieved the best annotation accuracy according to Kappa, mF1, and ACC.
193 The annotation accuracies of all other methods for the other tissue sections were slight worse
194 than for those when sample ID151507 was used as a reference (Supplementary Fig. 14a), which
195 is consistent with the simulations involving the misspecification of marker genes (Fig. 1d). This
196 suggests that annotation accuracy can be impaired when inaccurate marker genes are used.
197 However, this difference became negligible when the number of marker genes for each layer was
198 15. Furthermore, we examined the robustness of SpatialAnno using marker genes for irrelevant

199 cell types, those not present in the studied SRT dataset. For samples ID151669-151672 from
200 Donor 2, which only contained five cortical layers, we applied SpatialAnno and other methods
201 using marker genes for the seven layers. As shown in Supplementary Fig. 14b, SpatialAnno
202 achieved the best annotation performance for these samples.

203 Uniquely amongst the methods, SpatialAnno's estimated embeddings were highly informative
204 for the DLPFC layers in the 12 sections. The clustering accuracies, determined using the
205 ARI for embeddings from marker, non-marker, and a combination of the two, respectively,
206 were shown in Supplementary Fig. 14c, with the largest ARI value for embeddings from a
207 combination of the two. Clearly, embeddings from non-marker genes harbored substantial
208 amount of information about spatial domains, even more than the marker genes. When using
209 a combination of marker and non-marker genes, the embeddings led to improved clustering
210 performance, suggesting that annotation based on both marker and non-marker genes improved
211 the annotation accuracy. Red/green/blue (RGB) plots using three tSNE components for the
212 embeddings in sample ID151673 estimated by SpatialAnno revealed a more clear laminar
213 structure for DLPFC than those by PCA or DR-SC (Fig. 2d). Such stronger structure
214 predictivity from SpatialAnno is numerically supported by its higher ARI (0.450) compared to
215 PCA (ARI=0.296) and DR-SC (ARI=0.365). Moreover, an estimated PAGA graph²² using
216 SpatialAnno embeddings demonstrated the almost linear development trajectory from WM
217 to layer 1, while the PAGA graphs using both PCA and DR-SC embeddings were less clearly
218 delineated (Fig. 2e and Supplementary Fig. 2-13).

219 **SpatialAnno correctly identifies cells in mouse olfactory bulb**

220 To quantitatively demonstrate the performance of SpatialAnno compared with SCINA, scSorter,
221 CellAssign, and Garnett in domain-type annotation, we analyzed one mouse OB data generated
222 using ST technology. This dataset represented 12 tissue sections with a median of 16,024 gene
223 expression measurements among a median of 266 spots (Supplementary Table 2).

224 Taking the four anatomic layers manually annotated based on H&E staining as ground
225 truth (Fig. 3a), we first evaluated the performance of the spatial annotation using Kappa, mF1,
226 and ACC for section 12 (Fig. 3b). SpatialAnno annotated spatial domains more accurately
227 (Kappa=0.739, mF1 = 0.812, and ACC=0.800) than scSorter (Kappa=0.608, mF1=0.718, and
228 ACC=0.696), SCINA (Kappa=0.598, mF1=0.670, and ACC=0.689), CellAssign (Kappa=0.395,
229 mF1=0.607, and ACC=0.707), and Garnett (Kappa=0.552, mF1=0.686, and ACC=0.646). We
230 examined the robustness of SpatialAnno by including marker genes for two irrelevant cell types
231 (endothelial and mural cells) that were not present in this section, and SpatialAnno achieved
232 the best annotation performance (Supplementary Fig. 15a). To illustrate the effectiveness of
233 leveraging non-marker information, we evaluated the performance of the spatial annotation
234 by SpatialAnno, scSorter, and Garnett with 30, 300, or 3000 non-marker genes, as only these
235 three methods are able to leverage non-marker gene information. SpatialAnno achieved higher
236 annotation accuracy when more non-marker genes were used, while the difference in performance
237 between 300 and 3000 non-marker genes was minimal for SpatialAnno (Supplementary Fig.
238 15b). In contrast, scSorter and Garnett performed similarly with 30 or 300 non-marker genes,
239 but their performance deteriorated when 3000 non-marker genes were applied.

240 SpatialAnno recovered the laminar structure of the mouse OB across 12 sections (Supple-

241 mentary Fig. 16). The mouse OB has a multi-layered cellular architecture in the order, from
242 the inner to outer layer, of granule cell layer (GCL), mitral cell layer (MCL), glomerular layer
243 (GL), the nerve layer (ONL). Detailed assignments by SpatialAnno and the other four methods
244 for section 12 are shown in Fig. 3a. The cell types annotated by SpatialAnno accurately
245 represented this laminar structure, while CellAssign incorrectly assigned “unknown” cells to
246 regions belonging to GCL, MCL, and GL. Moreover, the annotation patterns of Garnett were
247 rather chaotic, while scSorter and SCINA failed to distinguish periglomerular cells (PGC) in
248 the GL.

249 We further examined the expressions of marker genes specific to each layer, including *Kit*
250 for external plexiform layer interneuron (EPL-IN)²³, *Penk* for granule cells (GC)²⁴, *Cdhr1*
251 for mitral and tufted cells (M/TC)²⁵, *S100a5* for olfactory sensory neurons (OSN)²⁶, and
252 *Th* for PGC²⁷ (Fig. 3c). Although the three methods provided similar assignments for GC,
253 M/TC, OSN, and PGC, their assignments for EPL-IN were quite different. EPL-IN are located
254 adjacent to GL in the external plexiform layer comprised of PGC²³. SpatialAnno assigned
255 spots near PGC to EPL-IN; however, scSorter and Garnett did not (Supplementary Fig. 17).
256 As the ground truth for the EPL-IN locations was unknown, we manually combined the inferred
257 EPL-IN with the adjacent layers in different ways: (1) by combining the inferred EPL-IN and
258 PGC and (2) by combining the inferred EPL-IN, M/TC, and PGC. SpatialAnno still achieved
259 the best annotation accuracy (Supplementary Fig. 15c & d).

260 Another key benefit of SpatialAnno is its ability to extract low-dimensional embeddings
261 relevant to different cell types from the high-dimensional non-marker genes, which is useful
262 for many downstream analyses. We summarized the low-dimensional embeddings inferred
263 by SpatialAnno (Supplementary Fig. 15e), PCA, and DR-SC into three-dimensional tSNE
264 components and visualized the resulting components in the RGB plot. The RGB plot (Fig. 3d)
265 shows the multi-layered architecture of the mouse OB, with neighboring spots sharing more
266 similar colors to those farther away. To compare the predictive powers of these low-dimensional
267 embeddings for the four anatomic layers annotated based on H&E staining, we applied the
268 Louvain community detection algorithm to spot clustering using the *Seurat* R package. The
269 clusters identified by SpatialAnno depicted the multi-layered structures more accurately (ARI
270 = 0.599) than those of PCA (ARI = 0.549) or DR-SC (ARI = 0.569).

271 **SpatialAnno reveals cell-type distribution in mouse hippocampus 272 with SRT data at near-cell resolution**

273 To show the cell-type distribution in the mouse hippocampus, we applied SpatialAnno and
274 the other methods to the analysis of a mouse hippocampus dataset generated using Slide-
275 seqV2, which quantifies transcriptome-wide expression levels at near-cellular resolution with
276 10- μ m barcoded beads³. This dataset contains expressions for 23,264 genes over 53,208 spatial
277 locations (Supplementary Table 3). As shown in the Allen Reference Atlas (Fig. 4a), the
278 primary regions in the mouse hippocampus were composed of the cornu ammonis (CA1-3) and
279 dentate gyrus (DG).

280 SpatialAnno clearly identified a “cord-like” structure as well as an “arrow-like” structure
281 in the hippocampal subfields in CA1, CA3, and DG (Fig. 4b), which is consistent with the
282 annotation of hippocampus structures in the Allen Reference Atlas (Fig. 4a). In contrast to

283 SpatialAnno, the other methods SCINA, Garnett, and CellAssign showed blurred/incorrect
284 localizations for the primary hippocampal subfields in CA3 and DG and were unable to reveal
285 the main structures of the mouse hippocampus (Fig. 4b and Supplementary Fig. 18-20).
286 The hippocampal subfields identified by scSorter were surrounded by a blurry border, with
287 many different cell types allocated to the same region. Additionally, all the methods except
288 SpatialAnno failed to accurately allocate the habenula (Hb)neurons, which should reside left to
289 and below the choroid plexus. Careful examination of marker genes further demonstrated the
290 superior accuracy of SpatialAnno (Fig. 4c), i.e., *Wfs1*, *Cpne4*, and *C1ql2* for CA1, CA3, and
291 DG, respectively.

292 We quantified the annotation performance of the different methods by examining the
293 correlations between the expression patterns of the marker genes and the three hippocampal
294 subfields identified by the different methods. Pearson's chi-squared test demonstrated a
295 substantial improvement in the magnitude of associations provided by SpatialAnno (Fig.
296 4d). The RGB plot for SpatialAnno displayed clear regional segregation of the hippocampus
297 (Supplementary Fig. 21a). Specifically, compared with the RGB plots for PCA and DR-SC,
298 the plot for SpatialAnno clearly depicted the Hb region.

299 Finally, we validated the cell-type distributions identified for an independent slide from the
300 mouse hippocampus profiled using Slide-seq. As with the initial version of Slide-seqV2, the
301 transcript detection sensitivity of Slide-seq is relatively low (Fig. 4e). By applying SpatialAnno
302 to this validation dataset, we showed the consistency of the cell-type distributions between
303 the two slides, as illustrated in Fig. 4f. SpatialAnno successfully identified the hippocampal
304 subfields in this Slide-seq data (Supplementary Fig. 21b-d and Supplementary Fig. 22-24).
305 The annotated regions for CA1, CA3, and DG with their marker gene expressions are shown in
306 Fig. 4g.

307 **Embeddings estimated by SpatialAnno lead to biologically relevant 308 trajectories in mouse embryo**

309 We further applied SpatialAnno and the other methods to the analysis of a dataset obtained
310 from three mouse embryo sections collated at the 8-12 somite stage using seqFISH², which has
311 the capability of probing the expression of a targeted gene set at the single-cell resolution².
312 Each of the three mouse embryo sections contained expression level measurements for 351 genes,
313 chosen to recover the cell-type identities at these developmental stages, from around 20,000
314 cells, as well as their physical locations (Supplementary Table 4). After selecting 168 marker
315 genes for 21 cell types (see Methods), 183 non-marker genes remained for annotation analysis.

316 The original study provided manual annotations for the cells based on their nearest neighbors
317 in the Gastrulation atlas²⁸. For each method, we summarized the annotation accuracy using
318 both Kappa, mF1 and ACC for each embryo section (Fig. 5a and Supplementary Fig. 25).
319 SpatialAnno achieved the highest Kappa, mF1 and ACC in two out of the three sections
320 and was only surpassed by CellAssign for the second embryo section. For Embryo 1, the
321 annotations of different methods are shown in Fig. 5b. Clearly, cell-type distributions identified
322 by SpatialAnno were well matched with the expression of their corresponding marker genes
323 (Fig. 5c).

324 For the embeddings uniquely estimated by SpatialAnno, we performed trajectory inference

325 on the brain cells to investigate the spatiotemporal development of the mouse brain and detected
326 two linear trajectories (Fig. 5d). We observed the lowest pseudotime values in the mesen-
327 cephalon, which diffused smoothly towards the tegmentum followed by the rhombencephalon in
328 one branch, and towards the prosencephalon in another branch (Fig. 5d). More importantly, the
329 diffusion patterns were spatially continuous and smooth. The detected trajectories delineated
330 the spatial trajectories of mouse brain development, which are in agreement with the findings
331 of recent studies^{2,29}. In contrast, the trajectories identified using embeddings from either PCA
332 or DR-SC lacked spatial continuity (Supplementary Fig. 26a & b). We further examined
333 genes associated with the inferred pseudotime, and a heatmap of the expression levels of the
334 top 20 significant genes suggested there were interesting expression patterns over pseudotime
335 (Supplementary Fig. 26c). A mesencephalon and prosencephalon marker gene, *Otx2*^{30,31}, showed
336 higher expression levels in the early stage of development, while at a later stage, its expression
337 levels were substantially suppressed (Supplementary Fig. 26d). In contrast, the expression levels
338 of a gene enriched in the rhombencephalon, *Sfrp1*³², changed from low to high (Supplementary
339 Fig. 26d). These results concur with the formation of the midbrain-hindbrain boundary^{33,34},
340 and this is supported by the observation that these two genes could be used to identify the
341 precise boundary between the mesencephalon and rhombencephalon (Supplementary Fig. 26e).

342 Discussion

343 SpatialAnno takes, as input, the normalized gene expression matrix, the physical location of
344 each spot, and a list of marker genes for known cell/domain types. The output of SpatialAnno
345 comprises the estimated posterior probability of each spot belonging to each cell/domain type
346 and the low-dimensional embeddings of each spot for non-marker genes. To efficiently capitalize
347 on both marker and non-marker genes, SpatialAnno uniquely models the expression levels of
348 non-marker genes via a factor model governed by cell/domain-type separable low-dimensional
349 embeddings and simultaneously promotes spatial smoothness via a Potts model. As a result,
350 SpatialAnno provides improved spatial cell/domain-type assignments, and its estimated low-
351 dimensional embeddings are cell-type-relevant and can facilitate downstream analyses such
352 as trajectory inference. SpatialAnno is computationally efficient, easily scalable to spatially
353 resolved transcriptomics with tens of thousands of spatial locations and thousands of genes
354 (Supplementary Table 5). With simulation studies, we demonstrated that SpatialAnno presents
355 improved spatial annotation accuracy with either correct, under- or over-specification of the
356 number of cell/domain types, robustness to the marker gene misspecification, and efficient
357 leveraging of non-marker genes compared with other annotation methods.

358 We examined the SRT data generated using different platforms, such as 10x Visium, ST,
359 Slide-seqV1/2, and seqFISH, with various spatial resolutions. Using both DLPFC 10x Visium
360 datasets and mouse OB ST datasets with manual annotations, we demonstrated the improved
361 annotation accuracy of SpatialAnno with the capability of recovering laminar structures, while
362 the identified PAGA graph using embeddings in SpatialAnno recovers an almost linear trajectory
363 from WM to layer 1. In DLPFC datasets, the domains identified were well matched with
364 the elevated expression for marker genes, such as *Pcp4* and *Mobp* that are marker genes
365 for layer 5 and WM, respectively^{20,21}, whereas *Pcp4* encodes Purkinje cell protein 4 and
366 *Mobp* encodes the myelin-associated oligodendrocyte basic protein. Using mouse hippocampus

367 Slide-seqV1/2 datasets, we demonstrated that SpatialAnno can successfully detect the primary
368 hippocampal subfields for CA1, CA3, and DG, with almost a perfect correlation between
369 cell-type proportions in both datasets and the elevated expression levels for *Wfs1*, *Cpne4*, and
370 *C1ql2* are well matched with CA1, CA3, and DG regions identified by SpatialAnno, respectively.
371 *Wfs1* showed differential expression in hippocampal field CA1 and has been reported to be
372 highly expressed in the CA1 region³⁵. *Cpne4*, a known marker gene for hippocampal subfield
373 CA3, was highly expressed in a region identified as CA3³⁶. In addition, *C1ql2*, a marker gene
374 for dentate principal cells, was expressed in a region identified as DG³⁷. When applied to mouse
375 embryo seqFISH datasets, SpatialAnno not only provided improved annotation accuracy, but
376 uniquely estimated cell-type-aware embeddings leading to the identification of two trajectories in
377 brain regions, originating in mesencephalon towards the rhombencephalon and prosencephalon,
378 respectively. Moreover, cell-type distributions identified by SpatialAnno were well matched
379 with the expression of their corresponding marker genes. For example, *Popdc2*, a cardiomyocyte
380 marker, was expressed in the developing heart tube³⁸. *Foxa1*, a gut endoderm marker, showed
381 the highest expression levels in the developing gut tube along the anterior–posterior axis of
382 the embryo³⁹. In addition, *Foxf1*, a mesoderm marker that encodes a forkhead transcription
383 factor expressed in the splanchnic mesenchyme surrounding the gut, was highly expressed at
384 the identified splanchnic mesoderm⁴⁰.

385 SpatialAnno paves the way for future spatial annotation analyses in multiple scenarios.
386 For example, a similar strategy can be applied to the problem of cell-type assignment in
387 other spatial omics data, such as spatial resolved single-cell chromatin accessibility data⁴¹ and
388 spatial proteomics⁴². To establish a complete spatial atlas of organism architecture, a critical
389 bottleneck is to perform an automatic cell-type assignment with both considerations of molecular
390 features with/without prior knowledge as well as their spatial organization, SpatialAnno can
391 substantially reduce both the irreproducibility and human effort in the processes of manual
392 cell/domain-type assignment⁴².

393 The benefits of SpatialAnno come with some caveats that may require further exploration.
394 First, SpatialAnno is applicable for spatial annotation in a single tissue slide. With multiple
395 tissue slides available, methods that are capable of integrating multiple SRT datasets for
396 cell/domain-type annotation are sincerely needed⁴³. Second, SpatialAnno was designed to
397 perform annotation analysis of data with a single modality. However, incorporating multi-modal
398 data with data of other modalities can further improve annotation accuracy. Third, many of
399 the early SRT technologies do not have a single-cell resolution, and SpatialAnno is only able to
400 assign domains with prior knowledge of each spot for those datasets. Cell-type annotation for
401 this type of dataset further requires simultaneous deconvolution with spatial cellular annotation.

402 Methods

403 SpatialAnno method overview

404 Probabilistic models for marker and non-marker gene expression

405 We herein present an overview of SpatialAnno, with its inference details provided in the
406 Supplementary Notes. SpatialAnno requires both spatial transcriptomics data and a list of

407 gene names for known cell/domain-type markers. The marker-gene list can be obtained from
 408 either the available publications, databases, or DEGs in scRNA-seq data (see Methods). In the
 409 SpatialAnno model, we denote X as the spot-by-gene expression matrix on n spatial locations.
 410 These locations have known spatial coordinates and unknown labels $y_i, i = 1, \dots, n$. We can
 411 separate genes into a group of m marker genes and a group of p non-marker genes, denoted as
 412 $\mathbf{x}_{1i} = (x_{i1}, \dots, x_{im})^\top$ and $\mathbf{x}_{2i} = (x_{i,m+1}, \dots, x_{i,m+p})^\top$, respectively. Suppose prior knowledge
 413 of marker genes for K cell/domain types is encoded as an indicator matrix ρ of dimension
 414 $m \times K$, with $\rho_{jk} = 1$ if gene j is a marker for cell/domain type k and 0 otherwise. Following^{44–46},
 415 we assume that the expression measurements have already been normalized through variance
 416 stabilizing transformation and further centered for each gene to have zero mean (see Methods).

417 SpatialAnno models the centered normalized expression vector, \mathbf{x}_{1i} , for marker genes in cell
 418 i , and latent label, y_i , as

$$\mathbf{x}_{1i} \mid y_i = k \sim \mathcal{N}(\boldsymbol{\mu}_{1k}, \Sigma_1), \quad (1)$$

$$\mu_{1jk} = \alpha_j + \rho_{jk}\beta_{jk},$$

419 with the constraint that $\beta_{jk} \geq 0$. Here, α_j is the base expression level for gene j in the marker
 420 group. The intuition is that if gene j is a marker for cell/domain type k , then we expect the
 421 expression of j to be higher in these cell/domain types¹⁴ with an increased magnitude β_{jk} . Note
 422 that there is no restriction stating marker genes cannot be expressed in other cell/domain types.
 423 We assume the covariance $\Sigma_1 = \text{diag}(\sigma_1^2, \dots, \sigma_m^2)$. This simplification significantly reduces the
 424 computational cost.

425 For the high-dimensional non-marker genes, SpatialAnno models their centered normalized
 426 expression vector, \mathbf{x}_{2i} , and latent label, y_i , as

$$\mathbf{x}_{2i} \mid \mathbf{z}_i = L\mathbf{z}_i + \mathbf{e}_i, \quad (2)$$

$$\mathbf{z}_i \mid y_i = k \sim \mathcal{N}(\mathbf{m}_k, V),$$

427 where factor $\mathbf{z}_i \in R^q$ represents a q -dimensional embedding of \mathbf{x}_{2i} ; L is a $p \times q$ factor loading
 428 matrix; $\mathbf{m}_k \in R^q$ is the mean vector for the k th cell/domain type, and V is the covariance
 429 matrix that is shared across cell/domain types; and \mathbf{e}_i is the residual error and follows an
 430 independent normal distribution with mean zero and variance Λ , which is a diagonal matrix,
 431 or $\mathbf{e}_i \sim \mathcal{N}(0, \Lambda)$.

432 Potts model for cell/domain labels

433 In the analysis of SRT datasets, the neighboring locations on the same tissue section often
 434 have similar cell/domain types. Thus, spots in neighboring locations contain immense amounts
 435 of information for annotating locations of interest. To promote neighborhood similarity in
 436 cell/domain types, we follow previous computation^{19,47} and assume that cell/domain type
 437 $y_i \in \{1, \dots, K\}$ follows a Potts model characterized by an interaction parameter ξ and a
 438 neighborhood graph \mathcal{S} ,

$$p(\mathbf{y} \mid \mathcal{S}, \xi) = \frac{1}{C(\xi)} \exp \left\{ -\xi \sum_{i \sim i'} [1 - I(y_i = y_{i'})] \right\}, \quad (3)$$

439 where $i \sim i'$ denotes all neighboring pairs in the neighborhood graph \mathcal{S} ; $I(y_i = y_{i'})$ is an indicator
 440 function that equals 1 if both the i th and i' th locations belong to the same cell/domain type
 441 and equals 0 otherwise; ξ is an unknown interaction parameter that determines the extent of
 442 cell/domain type similarity among neighboring locations; and $C(\xi)$ is the normalizing constant,
 443 also known as the partition function that ensures the above probability mass function has a
 444 summation of one across all possible configurations of \mathbf{y} .

445 SpatialAnno modulates the over-expression of marker genes in Equation (1), the high-
 446 dimensional non-marker gene expressions in Equation (2), and the spatial smoothness across
 447 spots with a Potts model in Equation (3). The hierarchical probabilistic framework of Spa-
 448 tialAnno enables us to develop an efficient optimization algorithm through restricted expectation-
 449 maximization (EM)⁴⁸ to estimate the probability of each location of a given cell/domain type.
 450 Briefly, our algorithm treats all parameters $\boldsymbol{\theta} = (\{\alpha_j\}, \{\beta_{jk}\}, \{\sigma_j^2\}, \xi, \mathbf{m}, V, L, \Lambda)$ as unknown
 451 and estimates these parameters based on the data at hand to ensure optimal annotation
 452 performance. Algorithm details are provided in the Supplementary Notes.

453 SpatialAnno has several advantages that facilitate highly accurate assignments and various
 454 downstream analyses of spatial transcriptomics. First, by modelling the spatial correlation
 455 as labels, SpatialAnno borrows the cell-type information across spatial locations for spatially
 456 informed cell/domain type annotation. Second, SpatialAnno models the high-dimensional
 457 expression values of non-marker genes with the factor model, which can efficiently utilize the
 458 expression of non-marker genes to help verify and adjust label assignments. Third, modelling
 459 the high-dimensional expression values of non-marker genes allows SpatialAnno to infer cell-
 460 type-relevant embeddings, facilitating effective spatial transcriptomics visualization and spatial
 461 trajectory inference.

462 Spatial annotation and cell/domain relevant embeddings

To leverage the spatial location information, we construct a neighborhood graph \mathcal{S} among locations by identifying the nearest neighbors for each spot. Specifically, the neighborhood N_i for a spot i is defined by applying a proximity threshold. Let \mathbf{y}_{N_i} denote the configurations of the neighbors of spot i . The probability that spot i is associated with cell/domain type k given $\mathbf{x}_{i1}, \mathbf{x}_{i2}$ and its neighbor configuration \mathbf{y}_{N_i} is specified by the following equation (Supplementary Notes) :

$$463 \quad \gamma_{ik} = C^{-1} p(\mathbf{x}_{i1} | y_i = k) p(\mathbf{x}_{i2} | y_i = k) p(y_i = k | \mathbf{y}_{N_i}), \quad (4)$$

463 where C is a normalization constant. In the right-hand side, $p(\mathbf{x}_{i1} | y_i = k)$ and $p(\mathbf{x}_{i2} | y_i = k)$
 464 model the effect of the expression levels of marker and non-marker genes, respectively, whereas
 465 $p(y_i = k | \mathbf{y}_{N_i})$ accounts for the effect of the neighbor configuration. The last term is determined
 466 by Eq. (3).

A key feature of SpatialAnno is its ability to extract cell/domain relevant embeddings for each spot. By modelling the expression levels of non-marker genes with factor models, SpatialAnno can extract cell/domain-type aware embeddings that can facilitate downstream analyses. Based on Eq. (2) and Bayes' theorem, the conditional distribution of latent factors \mathbf{z}_i given $(\mathbf{x}_{i1}, \mathbf{x}_{i2}, y_i = k)$ follows a multivariate normal distribution $\mathcal{N}(\mathbf{w}_{ik}, M)$ with mean \mathbf{w}_{ik} and variance M (Supplementary Notes). The low-dimensional embeddings for spot i are

estimated by the posterior expectation of its latent factors \mathbf{z}_i :

$$E(\mathbf{z}_i | \mathbf{x}_{i1}, \mathbf{x}_{i2}, \mathbf{y}_{N_i}) = \sum_k \gamma_{ik} \mathbf{w}_{ik}, \quad (5)$$

which are weighted averages that take into account the relative importance of each type. In this way, the embeddings are encouraged to be label-relevant.

Compared methods and evaluation metrics

On all the simulated datasets and real datasets, we compared SpatialAnno with four annotation methods: (1) SCINA¹² implemented in the R package *SCINA* (version 1.2.0); (2) Garnett¹³ implemented in the R package *garnett* (version 0.1.21); (3) CellAssign¹⁴ implemented in the R package *cellassign* (version 0.99.21); and (4) scSorter¹⁵ implemented in the R package *scSorter* (version 0.0.2). We used the recommended default parameter settings in their tutorials. Among these methods, SCINA and CellAssign only use the expression of marker genes, and scSorter and Garnett can borrow information from the expression of non-marker genes. We evaluated the annotation performance using three metrics, i.e., Kappa, mF1 score, and ACC, as suggested in previous annotation studies of single-cell data^{11,49}. ACC was defined as the proportion of spots that were classified into the correct types. Kappa is generally thought to be a more robust measure than ACC, as it takes into account the possibility of the agreement occurring by chance. The cell-level F1 score considers each cell to be an individual classification task with a true cell-type assignment (and potentially multiple incorrect cell-type assignments) for the purposes of calculating precision and recall (Supplementary Notes).

We also compared the low-dimensional embeddings estimated in SpatialAnno with those from PCA and DR-SC¹⁹. In detail, we first extracted the top 15-dimensional components and then summarized those top components as three tSNE components and visualizing the resulting tSNE components with RGB colors in the RGB plot. To show that the estimated embeddings carry the most information about cell/domain types, we evaluated the conditional correlation coefficients between the true cell/domain labels and the observed gene expression, given the estimated embeddings in SpatialAnno. Furthermore, the embeddings in SpatialAnno improve clustering performance. With embeddings from SpatialAnno, PCA, and DR-SC, we performed clustering analysis using the Louvain community detection algorithm implemented in the R package *Seurat* (version 4.1.1), and evaluated clustering performance using the ARI⁵⁰.

Simulations

We performed comprehensive simulations to evaluate the performance of SpatialAnno and compared it with that of alternative annotation methods. The spatial locations of 3639 spots were taken from DLPFC section 151673. Cell/domain types were assigned with the manually annotations from the original studies²⁰. We simulated gene expression data for each spot using the *splatter* package (version 1.20.0). The parameter for the proportion of DEGs (*de.prob*) in each layer was set to 0.5. The DE strength was determined by both the mean parameter *de.facloc* and scale parameter *de.facScale*, the former ranges from 0.1 to 0.8, and the latter was set to within [0.1,1], corresponding to the log fold change in expression from one-fold to

503 two-fold across different types. All the other parameters were set based on their estimates in
504 the seven layers from DLPFC section 151673.

505 Five marker genes for each cell/domain type were selected from the top DEGs based on
506 log-fold change in expression. We tested the accuracy and robustness of SpatialAnno with the
507 following settings that reflect real-world scenarios.

508 I. To test the robustness of SpatialAnno to the erroneous specification of the number of
509 cell/domain types, we considered three scenarios. In the first scenario, marker genes for
510 all seven cell/domain types were provided and no unknown cell/domain types existed
511 in the expression data. In the second scenario, marker genes for two cell/domain types
512 were removed to create a scenario in which fewer cell/domain types were specified in
513 the marker gene matrix than actually exist in the data. Thus, cells from these two
514 cell/domain types should be assigned to "unknown". In the third scenario, the marker
515 genes for nine cell/domain types were added, but two cell/domain types did not appear
516 in the expression data. This mimics a scenario in which there are more cell/domain types
517 are specified in the marker gene matrix than actually exist in the data.

518 II. To evaluate the robustness of SpatialAnno to the marker gene misspecification, we next
519 created a scenario in which marker genes may be incomplete or incorrect. We randomly
520 flipped a fraction of entries in the binary marker gene matrix ρ to introduce errors.
521 Specifically, the procedure consisted of two steps. In the first step, a proportion of entries
522 in ρ that contained one were flipped. In the second step, the same number of entries
523 flipped in the first step were flipped for the entries that contained zero in the original ρ .
524 The considered proportions were set to be either 10%, 20%, or 30%. Other settings were
525 similar to those in the first scenario in Simulation I.

526 III. To assess the capability of SpatialAnno to utilize high-dimensional non-marker genes, we
527 varied the number of non-marker genes as 60, 100, 500, 1000, and 2000. In this setting,
528 we only compared scSorter and Garnett, as only these methods can utilize non-marker
529 genes. Other settings were similar to those in the first scenario in Simulation I.

530 For each simulation setting, we performed 50 replicate simulations. In each replicate, we applied
531 SpatialAnno and the other methods to annotate each spot.

532 Data analysis

533 Normalization of SRT data

534 For all datasets, we normalized the raw expression count matrix using the variance stabilizing
535 transformation function, **SCTransform**, provided in *Seurat* (version 4.1.1). We performed gene
536 filtering using *SPARK* (version 1.1.1)⁵¹ for data with transcriptome-wide measurements. The
537 most spatially variable genes (see Data resource) were selected as input for the annotation
538 methods SpatialAnno, scSorter, SCINA, and Garnett. CellAssign took the raw count matrix of
539 these genes as input.

540 **Selection of marker genes**

541 We obtained a marker gene list primarily following the protocols of CellAssign. We (1) performed
542 differential expression analysis of a reference scRNA-seq/SRT data using the **FindAllMarkers**
543 function in the R package *Seurat* (version 4.1.1) and selected the top 30 DEGs ordered by the
544 log₂(fold-change) with upregulation, (2) removed those with an insignificant adjusted *p*-value
545 and those detection percentages across different cell/domain types were similar (differences
546 between pct.1 and pct.2 values from the **FindAllMarkers** function are lower than 0.3), and (3)
547 filtered out genes that were of low expression in the spatial transcriptomic data. We finally
548 selected the top-ranked genes with the smallest *p*-values.

549 **Clustering analysis**

550 To examine the information captured by SpaitalAnno embeddings of non-marker genes, we
551 performed clustering analysis using three different sets of embeddings as input in both the
552 simulated and DLPFC data. The three embedding sets include the top 15 PCs in marker genes
553 by PCA, 15-dimensional embeddings in non-marker genes by SpatialAnno, and combined. We
554 then performed clustering analysis using the Louvain community detection algorithm.

555 **Spatial trajectory inference**

556 To construct a spatial map of the DLPFC Visium data, we employed the PAGA algorithm²²
557 implemented in the Python package *SCANPY* (version 1.9.1) to preserve the global topology
558 in the embeddings of non-marker genes. The cluster labels for PCA embeddings and DR-SC
559 embeddings were estimated using the spatial clustering methods implemented in the R packages
560 *BayesSpace* (version 1.5.1)⁵² and *DR-SC* (version 2.9.0)¹⁹, respectively.

561 To estimate the developmental trajectories among the various locations in the brain regions,
562 we applied Slingshot⁵³ to the low-dimensional embeddings. As SpatialAnno only extracts
563 embeddings of non-marker genes, we combined them with the embeddings of marker genes by
564 PCA. The cluster labels used in Slingshot were obtained from the spatial clustering method DR-
565 SC¹⁹. To detect DEGs along the estimated pseudotime, we used the function **testPseudotime**
566 in the R package *TSCAN* (version 1.37.0)⁵⁴.

567 **Data resources**

568 **Human dorsolateral prefrontal cortex data obtained by 10x Visium**

569 We downloaded a human DLPFC data set²⁰ that was generated by the 10x Visium platform
570 from <http://spatial.libd.org/spatialLIBD/>. In this dataset, there were 12 tissue sections,
571 which contained a total of 33,538 genes measured on average over 3973 spots. We used the
572 sample ID151673, which contains expression measurements of 33,538 genes on 3639 spots,
573 as the main analysis example. We presented the results for the other 11 samples in the
574 Supplementary Figures. For all the sections, we extracted the top 2000 spatially variable genes
575 with SPARK-X⁵¹ before performing annotations.

576 To identify layer-specific marker genes for annotation, we used tissue section 151507 as the
577 reference data. This dataset contained 33,538 genes for 4,226 spots. For each layer, the top 5

578 DEGs were selected as its marker genes. The final marker gene list is available in Supplementary
579 Table 6.

580 **Mouse olfactory bulb data by spatial transcriptomics (ST)**

581 We obtained the mouse olfactory bulb ST data from the spatial transcriptomics research website
582 (<https://www.spatialresearch.org/>). This data consists of gene expression levels in the
583 form of read counts that were collected for a number of spatial locations. We followed the
584 methods of previous studies^{55,56} to focus on the mouse OB section 12, which contains 16,034
585 genes and 282 spatial locations. We presented the results for the other 11 sections in the
586 Supplementary Figures. We extracted the top 3000 most highly variable genes with function
587 **SCTransform** implemented in *Seurat* (version 4.0.5)⁵⁷ before performing annotations.

588 To construct the marker gene list for annotation, we perform differential expression analysis
589 on scRNA-seq data²³ from the Gene Expression Omnibus (GEO; accession number GSE121891).
590 This scRNA-seq data was collected from the mouse olfactory bulb and contains 18,560 genes
591 and 12,801 cells for five cell types: granule cells (GC, $n=8614$), olfactory sensory neurons
592 (OSNs, $n = 1200$), periglomerular cells (PGC, $n = 1693$), mitral and tufted cells (M-TC, $n =$
593 1133), and external plexiform layer interneurons (EPL-IN, $n = 161$). For each cell type, the
594 top four DEGs were selected as its marker genes. The final marker gene list is available in
595 Supplementary Table 7.

596 **Mouse hippocampus Slide-seq data and Slide-seqV2 data**

597 We obtained the mouse hippocampus Slide-seq dataset and Slide-seqV2 dataset³ from the
598 Broad Institute's Single Cell Portal (https://singlecell.broadinstitute.org/single_cell/study/SCP948/robust-decomposition-of-cell-type-mixtures-in-spatial-transcriptomics).
600 The Slide-seq dataset consists of gene expression measurements in the form of read counts for
601 22,457 genes and 34,199 spatial locations. The Slide-seqV2 dataset consists of gene expression
602 measurements in the form of read counts for 23,264 genes and 53,208 spatial locations. In the
603 analysis, we filtered out genes that had fewer than 20 counts on all locations and filtered out
604 locations that had fewer than 20 genes with nonzero counts. These filtering criteria led to final
605 sets of 14,481 genes and 31,664 cells for Slide-seq dataset, and 16,121 genes and 51,212 cells for
606 Slide-seqV2 dataset. In addition, for both datasets, we extracted the top 2000 most spatially
607 variable genes with SPARK-X⁵¹ before performing annotations.

608 To construct marker genes for annotation, we obtained the DropViZ scRNA-seq dataset⁵⁸
609 from the Broad Institute's Single Cell Portal. This data was collected from the mouse
610 hippocampus, which contained 22,245 genes and 52,846 cells for 19 cell types. For each cell
611 type, the top five DEGs were selected as marker genes. Besides the 19 cell types, we added
612 another two cell types, *Slc17a6* neurons and Hb neurons, and their marker genes were extracted
613 from the original study⁵⁸. The final marker gene list used is available in Supplementary Table
614 8.

615 Mouse embryo data by seqFISH

616 We obtained the mouse embryo seqFISH data² from <https://marionilab.cruk.cam.ac.uk/SpatialMouseAtlas/>. This dataset consists of 387 selected target genes from three mouse
617 embryo tissue sections for 19,451, 14,891, and 23,194 cells, respectively. We calculated
618 normalized expression log counts for each cell using `logNormCounts` function in the R package
619 `scuttle`⁵⁹ with cell-specific size factors.

621 To construct the marker gene list, we used Embryo 3 as a reference; this dataset contains 24
622 cell types. For each cell type, the top eight DEGs were selected as marker genes. We removed
623 marker genes for two cell types, ExE endoderm cells and blood progenitors, as there were too
624 few (less than 30) of these cells. The cell type “Low quality” was also removed. The final
625 marker gene list used contained 21 cell types and is available in Supplementary Table 9.

626 Data availability

627 This study made use of publicly available datasets. These include the mouse OB dataset
628 (<https://www.spatialresearch.org/>), DLPFC dataset on the 10x Visium platform are ac-
629 cessible at (<https://github.com/LieberInstitute/spatialLIBD>), seqFISH dataset (<https://doi.org/10.18129/B9.bioc.MouseGastrulationData>), and mouse hippocampus Slide-seq
630 and Slide-seqV2 datasets (https://singlecell.broadinstitute.org/single_cell/study/SCP948/robust-decomposition-of-cell-type-mixtures-in-spatial-transcriptomics).
632

633 Code availability

634 The SpatialAnno software and source code have been deposited at <https://github.com/Shufeyangyi2015310117/SpatialAnno>. Example codes for using SpatialAnno are publicly
635 available at <https://shufeyangyi2015310117.github.io/SpatialAnno/index.html>. All
636 scripts used to reproduce all the analyses can be found at https://github.com/Shufeyangyi2015310117/SpatialAnno_Analysis and <https://doi.org/10.5281/zenodo.7413083>.
638

639 Author contributions

640 X.S. and J.L. initiated and designed the study. X.S. and Y.Y. developed the method, imple-
641 mented the software, performed simulations and analyzed real data. X.S. and J.L. wrote the
642 manuscript, and all authors edited and revised the manuscript.

643 Competing interests

644 The authors declare no competing interests.

645 References

646 [1] Moffitt, J. R. *et al.* Molecular, spatial, and functional single-cell profiling of the hypotha-
647 lamic preoptic region. *Science* **362**, eaau5324 (2018).

648 [2] Lohoff, T. *et al.* Integration of spatial and single-cell transcriptomic data elucidates mouse
649 organogenesis. *Nature biotechnology* **40**, 74–85 (2022).

650 [3] Stickels, R. R. *et al.* Highly sensitive spatial transcriptomics at near-cellular resolution
651 with slide-seqv2. *Nature biotechnology* **39**, 313–319 (2021).

652 [4] Chen, A. *et al.* Spatiotemporal transcriptomic atlas of mouse organogenesis using dna
653 nanoball-patterned arrays. *Cell* **185**, 1777–1792 (2022).

654 [5] Palla, G., Fischer, D. S., Regev, A. & Theis, F. J. Spatial components of molecular tissue
655 biology. *Nature Biotechnology* **40**, 308–318 (2022).

656 [6] Lähnemann, D. *et al.* Eleven grand challenges in single-cell data science. *Genome biology*
657 **21**, 1–35 (2020).

658 [7] Franzén, O., Gan, L.-M. & Björkegren, J. L. Panglaodb: a web server for exploration of
659 mouse and human single-cell rna sequencing data. *Database* **2019** (2019).

660 [8] Zhang, X. *et al.* Cellmarker: a manually curated resource of cell markers in human and
661 mouse. *Nucleic acids research* **47**, D721–D728 (2019).

662 [9] Clarke, Z. A. *et al.* Tutorial: guidelines for annotating single-cell transcriptomic maps
663 using automated and manual methods. *Nature protocols* **16**, 2749–2764 (2021).

664 [10] Duò, A., Robinson, M. D. & Soneson, C. A systematic performance evaluation of clustering
665 methods for single-cell rna-seq data. *F1000Research* **7** (2018).

666 [11] Kiselev, V. Y., Yiu, A. & Hemberg, M. scmap: projection of single-cell rna-seq data across
667 data sets. *Nature methods* **15**, 359–362 (2018).

668 [12] Zhang, Z. *et al.* Scina: a semi-supervised subtyping algorithm of single cells and bulk
669 samples. *Genes* **10**, 531 (2019).

670 [13] Pliner, H. A., Shendure, J. & Trapnell, C. Supervised classification enables rapid annotation
671 of cell atlases. *Nature methods* **16**, 983–986 (2019).

672 [14] Zhang, A. W. *et al.* Probabilistic cell-type assignment of single-cell rna-seq for tumor
673 microenvironment profiling. *Nature methods* **16**, 1007–1015 (2019).

674 [15] Guo, H. & Li, J. scsorter: assigning cells to known cell types according to marker genes.
675 *Genome biology* **22**, 1–18 (2021).

676 [16] Wu, F.-Y. The potts model. *Reviews of modern physics* **54**, 235 (1982).

677 [17] Zhang, Y., Brady, M. & Smith, S. Segmentation of brain mr images through a hid-
678 den markov random field model and the expectation-maximization algorithm. *IEEE*
679 *transactions on medical imaging* **20**, 45–57 (2001).

680 [18] Zappia, L., Phipson, B. & Oshlack, A. Splatter: simulation of single-cell rna sequencing
681 data. *Genome biology* **18**, 1–15 (2017).

682 [19] Liu, W. *et al.* Joint dimension reduction and clustering analysis of single-cell rna-seq and
683 spatial transcriptomics data. *Nucleic acids research* **50**, e72–e72 (2022).

684 [20] Maynard, K. R. *et al.* Transcriptome-scale spatial gene expression in the human dorsolateral
685 prefrontal cortex. *Nature neuroscience* **24**, 425–436 (2021).

686 [21] Molyneaux, B. J., Arlotta, P., Menezes, J. R. & Macklis, J. D. Neuronal subtype
687 specification in the cerebral cortex. *Nature reviews neuroscience* **8**, 427–437 (2007).

688 [22] Wolf, F. A. *et al.* Paga: graph abstraction reconciles clustering with trajectory inference
689 through a topology preserving map of single cells. *Genome biology* **20**, 1–9 (2019).

690 [23] Tepe, B. *et al.* Single-cell rna-seq of mouse olfactory bulb reveals cellular heterogeneity and
691 activity-dependent molecular census of adult-born neurons. *Cell reports* **25**, 2689–2703
692 (2018).

693 [24] Erwin, S. R. *et al.* A sparse, spatially biased subtype of mature granule cell dominates
694 recruitment in hippocampal-associated behaviors. *Cell reports* **31**, 107551 (2020).

695 [25] Nagai, Y., Sano, H. & Yokoi, M. Transgenic expression of cre recombinase in mitral/tufted
696 cells of the olfactory bulb. *genesis* **43**, 12–16 (2005).

697 [26] van der Linden, C. J. *et al.* Olfactory stimulation regulates the birth of neurons that
698 express specific odorant receptors. *Cell reports* **33**, 108210 (2020).

699 [27] Martín-López, E., Corona, R. & López-Mascaraque, L. Postnatal characterization of cells
700 in the accessory olfactory bulb of wild type and reeler mice. *Frontiers in Neuroanatomy* **6**,
701 15 (2012).

702 [28] Pijuan-Sala, B. *et al.* A single-cell molecular map of mouse gastrulation and early
703 organogenesis. *Nature* **566**, 490–495 (2019).

704 [29] Abdelaal, T., Lelieveldt, B. P., Reinders, M. J. & Mahfouz, A. Sirv: Spatial inference of
705 rna velocity at the single-cell resolution. *bioRxiv* (2021).

706 [30] Simeone, A., Acampora, D., Gulisano, M., Stornaiuolo, A. & Boncinelli, E. Nested
707 expression domains of four homeobox genes in developing rostral brain. *Nature* **358**,
708 687–690 (1992).

709 [31] Bouillet, P., Chazaud, C., Oulad-Abdelghani, M., Dollé, P. & Chambon, P. Sequence and
710 expression pattern of the stra7 (gbx-2) homeobox-containing gene induced by retinoic acid
711 in p19 embryonal carcinoma cells. *Developmental Dynamics* **204**, 372–382 (1995).

712 [32] Leimeister, C., Bach, A. & Gessler, M. Developmental expression patterns of mouse sfrp
713 genes encoding members of the secreted frizzled related protein family. *Mechanisms of*
714 *development* **75**, 29–42 (1998).

715 [33] Wurst, W. & Bally-Cuif, L. Neural plate patterning: upstream and downstream of the
716 isthmic organizer. *Nature Reviews Neuroscience* **2**, 99–108 (2001).

717 [34] Raible, F. & Brand, M. Divide et impera—the midbrain–hindbrain boundary and its
718 organizer. *Trends in neurosciences* **27**, 727–734 (2004).

719 [35] Dong, H.-W., Swanson, L. W., Chen, L., Fanselow, M. S. & Toga, A. W. Genomic–
720 anatomic evidence for distinct functional domains in hippocampal field ca1. *Proceedings*
721 *of the National Academy of Sciences* **106**, 11794–11799 (2009).

722 [36] Arneson, D. *et al.* Single cell molecular alterations reveal target cells and pathways of
723 concussive brain injury. *Nature communications* **9**, 1–18 (2018).

724 [37] Matsuda, K. *et al.* Transsynaptic modulation of kainate receptor functions by c1q-like
725 proteins. *Neuron* **90**, 752–767 (2016).

726 [38] Breher, S. S. *et al.* Popeye domain containing gene 2 (popdc2) is a myocyte-specific
727 differentiation marker during chick heart development. *Developmental dynamics: an*
728 *official publication of the American Association of Anatomists* **229**, 695–702 (2004).

729 [39] Sasaki, H. & Hogan, B. Differential expression of multiple fork head related genes during
730 gastrulation and axial pattern formation in the mouse embryo. *Development* **118**, 47–59
731 (1993).

732 [40] Mahlapuu, M., Ormestad, M., Enerback, S. & Carlsson, P. The forkhead transcription
733 factor foxf1 is required for differentiation of extra-embryonic and lateral plate mesoderm.
734 *Development* **128**, 155–166 (2001).

735 [41] Deng, Y. *et al.* Spatial profiling of chromatin accessibility in mouse and human tissues.
736 *Nature* **609**, 375–383 (2022).

737 [42] Brbić, M. *et al.* Annotation of spatially resolved single-cell data with stellar. *Nature*
738 *Methods* 1–8 (2022).

739 [43] Liu, W. *et al.* Probabilistic embedding and clustering with alignment for spatial transcrip-
740 toomics data integration with precast. *bioRxiv* (2022).

741 [44] Zheng, G. X. *et al.* Massively parallel digital transcriptional profiling of single cells. *Nature*
742 *communications* **8**, 1–12 (2017).

743 [45] Butler, A., Hoffman, P., Smibert, P., Papalex, E. & Satija, R. Integrating single-
744 cell transcriptomic data across different conditions, technologies, and species. *Nature*
745 *biotechnology* **36**, 411–420 (2018).

746 [46] Hafemeister, C. & Satija, R. Normalization and variance stabilization of single-cell rna-seq
747 data using regularized negative binomial regression. *Genome biology* **20**, 1–15 (2019).

748 [47] Yang, Y. *et al.* Sc-meb: spatial clustering with hidden markov random field using empirical
749 bayes. *Briefings in bioinformatics* **23**, bbab466 (2022).

750 [48] Jamshidian, M. On algorithms for restricted maximum likelihood estimation. *Computa-*
751 *tional statistics & data analysis* **45**, 137–157 (2004).

752 [49] Chen, X. *et al.* Cell type annotation of single-cell chromatin accessibility data via supervised
753 bayesian embedding. *Nature Machine Intelligence* **4**, 116–126 (2022).

754 [50] Hubert, L. & Arabie, P. Comparing partitions. *Journal of classification* **2**, 193–218 (1985).

755 [51] Zhu, J., Sun, S. & Zhou, X. Spark-x: non-parametric modeling enables scalable and robust
756 detection of spatial expression patterns for large spatial transcriptomic studies. *Genome*
757 *biology* **22**, 1–25 (2021).

758 [52] Zhao, E. *et al.* Spatial transcriptomics at subspot resolution with bayesspace. *Nature*
759 *Biotechnology* **39**, 1375–1384 (2021).

760 [53] Street, K. *et al.* Slingshot: cell lineage and pseudotime inference for single-cell transcriptomics.
761 *BMC genomics* **19**, 1–16 (2018).

762 [54] Ji, Z. & Ji, H. Tscan: Pseudo-time reconstruction and evaluation in single-cell rna-seq
763 analysis. *Nucleic acids research* **44**, e117–e117 (2016).

764 [55] Ståhl, P. L. *et al.* Visualization and analysis of gene expression in tissue sections by spatial
765 transcriptomics. *Science* **353**, 78–82 (2016).

766 [56] Edsgård, D., Johnsson, P. & Sandberg, R. Identification of spatial expression trends in
767 single-cell gene expression data. *Nature methods* **15**, 339–342 (2018).

768 [57] Hao, Y. *et al.* Integrated analysis of multimodal single-cell data. *Cell* **184**, 3573–3587
769 (2021).

770 [58] Saunders, A. *et al.* Molecular diversity and specializations among the cells of the adult
771 mouse brain. *Cell* **174**, 1015–1030 (2018).

772 [59] Lun, A. T., McCarthy, D. J. & Marioni, J. C. A step-by-step workflow for low-level
773 analysis of single-cell rna-seq data with bioconductor. *F1000Research* **5** (2016).

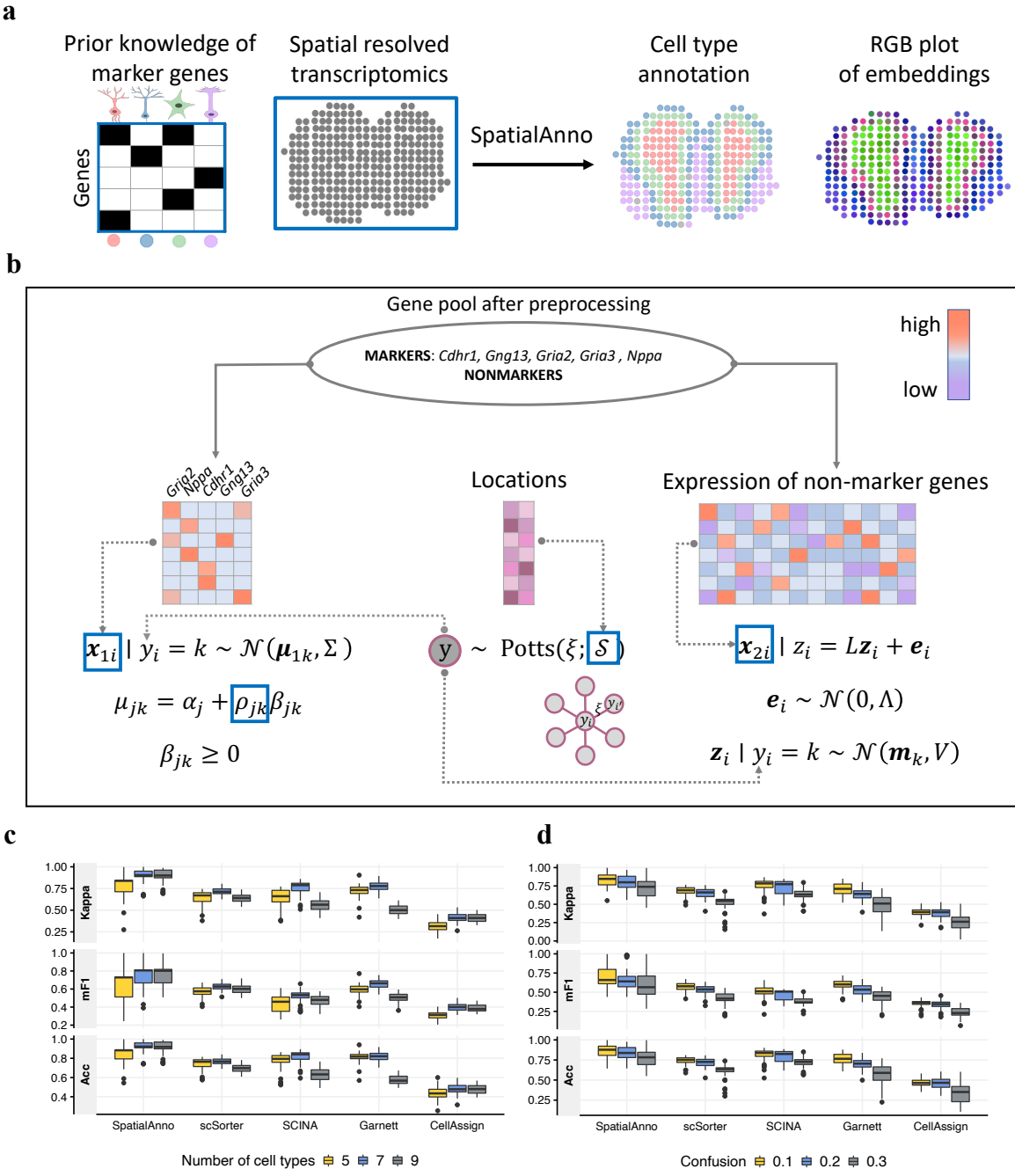


Figure 1: Schematic overview of SpatialAnno and its performance in simulation studies. **a** SpatialAnno employs spatial transcriptomics data along with a known marker-gene list in its analysis. With these two datasets as input, SpatialAnno performs spatial annotation via a probabilistic model that combines both marker and non-marker gene expression data, and produces both domain/cell-type assignments and low-dimensional embeddings for all spatial locations as output. **b** Overview of the SpatialAnno probabilistic model. Latent cell/domain types (shown in the grey circle) and observed data (shown in the blue boxes) are shown along with the distributional assumptions. **c** Kappa, mF1, and ACC of SpatialAnno, scSorter, SCINA, Garnett, and CellAssign for simulation data from seven cortical layers; different numbers of cell/domain types are provided as a list of marker genes. **d** Kappa, mF1 and ACC of SpatialAnno, scSorter, SCINA, CellAssign and Garnett for simulation data from seven cortical layers; different proportions of marker genes are erroneously specified.

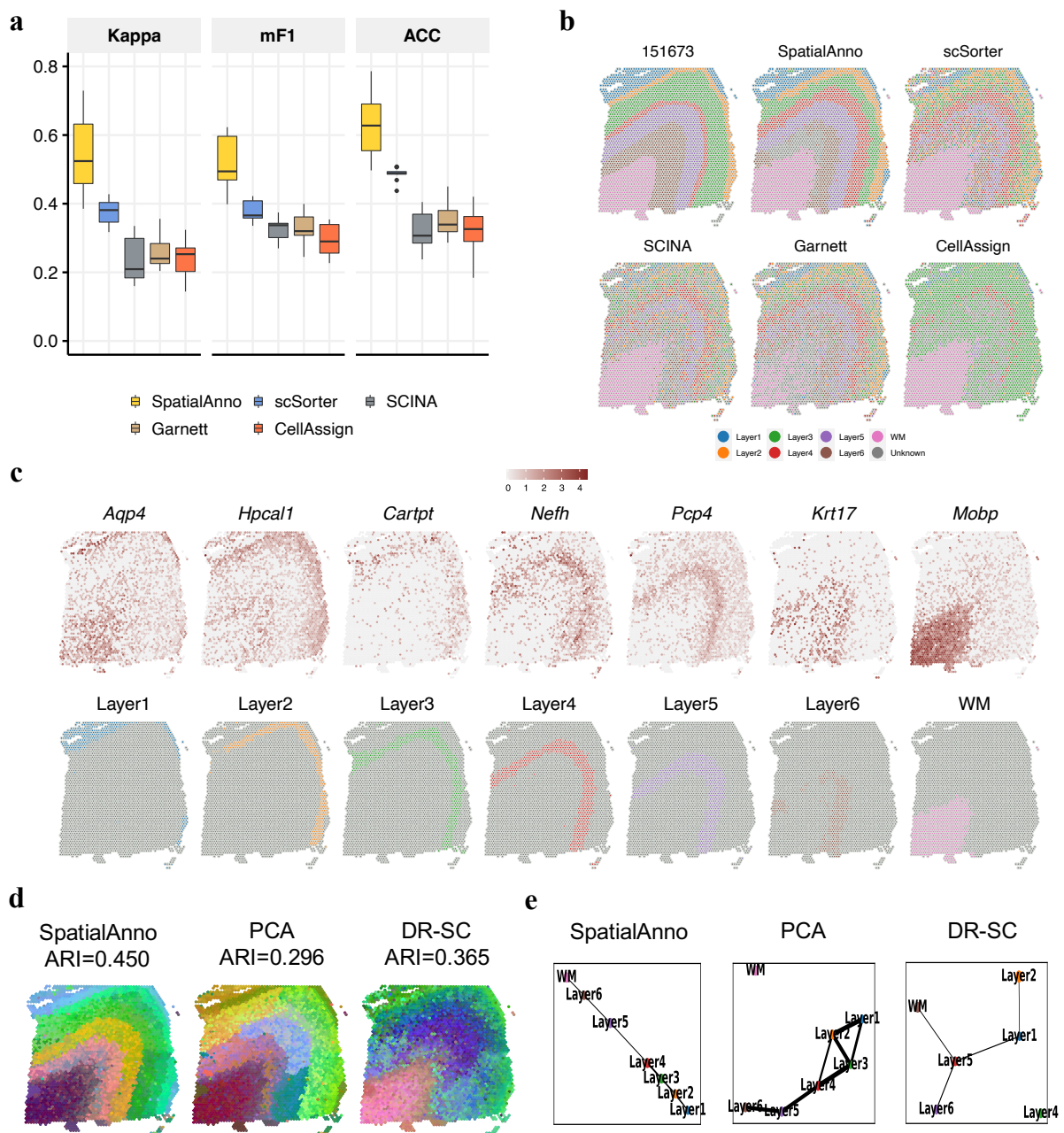


Figure 2: Spatial domain annotation in the DLPFC 10x Visium dataset. **a** Boxplots of Kappa, mF1, and ACC showing the accuracy of different methods for domain annotation across 12 tissue sections. **b** Spatial domain annotation in tissue sample ID151673 for ground truth, SpatialAnno, scSorter, SCINA, Garnett and CellAssign. **c** Top, expression levels of corresponding layer-specific marker genes. Bottom, annotations by SpatialAnno are shown on each spot. **d** RGB plots for low-dimensional embedding inferred by SpatialAnno, PCA, and DR-SC. As end-to-end annotation approaches, scSorter, SCINA, Garnett, and CellAssign cannot be utilized to extract low-dimensional embeddings. **e** PAGA graphs generated by SpatialAnno, PCA, and DR-SC embeddings for DLPFC Section ID151673.

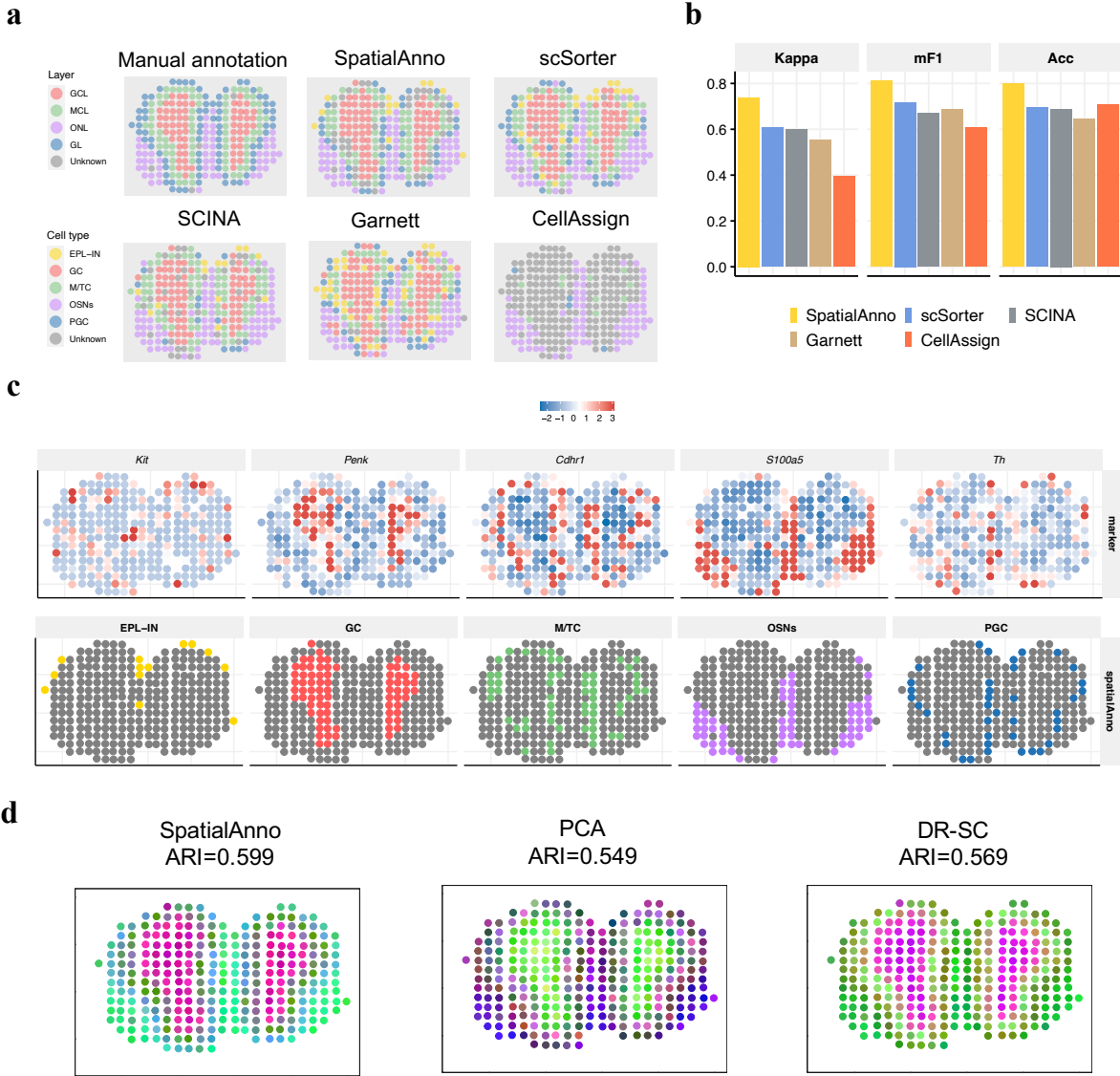


Figure 3: Spatial domain annotation in the mouse olfactory bulb dataset. **a** Spatial domain annotations for ground truth, SpatialAnno, scSorter, SCINA, Garnett, and CellAssign. **b** Bar plots of Kappa, mF1 and ACC showing the domain-type annotation accuracy of different methods. **c** Top, expression levels of corresponding cell-type-specific marker genes. Bottom, annotations by SpatialAnno are shown on each spot. **d**, RGB plots of low-dimensional embeddings inferred by SpatialAnno, PCA, and DR-SC. As end-to-end annotation approaches, scSorter, SCINA, Garnett, and CellAssign cannot be utilized to extract low-dimensional embeddings.

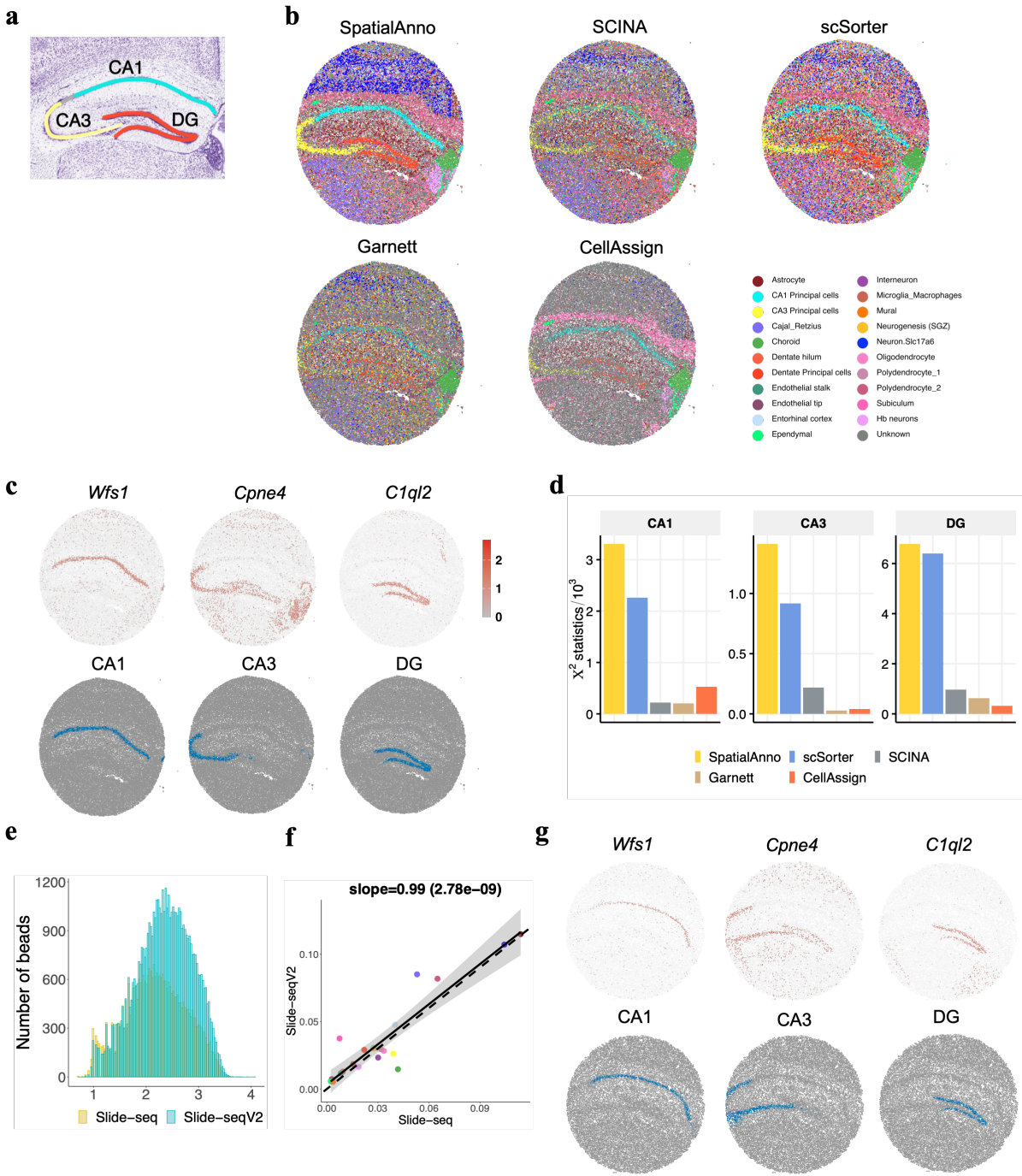


Figure 4: Spatial cell-type annotation of the mouse hippocampus dataset. **a** Annotation of hippocampus structures from the Allen Reference Atlas of an adult mouse brain. **b** Spatial annotation of the Slide-seqV2 hippocampus section by SpatialAnno, scSorter, SCINA, Garnett, and CellAssign. **c** Top, expression levels of corresponding cell-type-specific marker genes. Bottom, annotations by SpatialAnno of the Slide-seqV2 hippocampus section are shown on each spot. The examined cell types were CA1 cells, CA3 cells and dentate cells. **d** Results of Pearson's chi-squared test of correlation between expression patterns of marker genes and the three hippocampal subfields identified by different methods. **e** Total UMIs per bead for Slide-seq (yellow, $n = 34,199$ spots) versus Slide-seqV2 (blue, $n = 53,208$ spots) in the mouse hippocampus sections. **f** Scatter plot of cell-type proportions identified by SpatialAnno in Slide-seq and Slide-seqV2 datasets. **g** Top, expression levels of corresponding cell type specific marker genes. Bottom, annotation by SpatialAnno of the Slide-seq hippocampus section is shown on each spot.

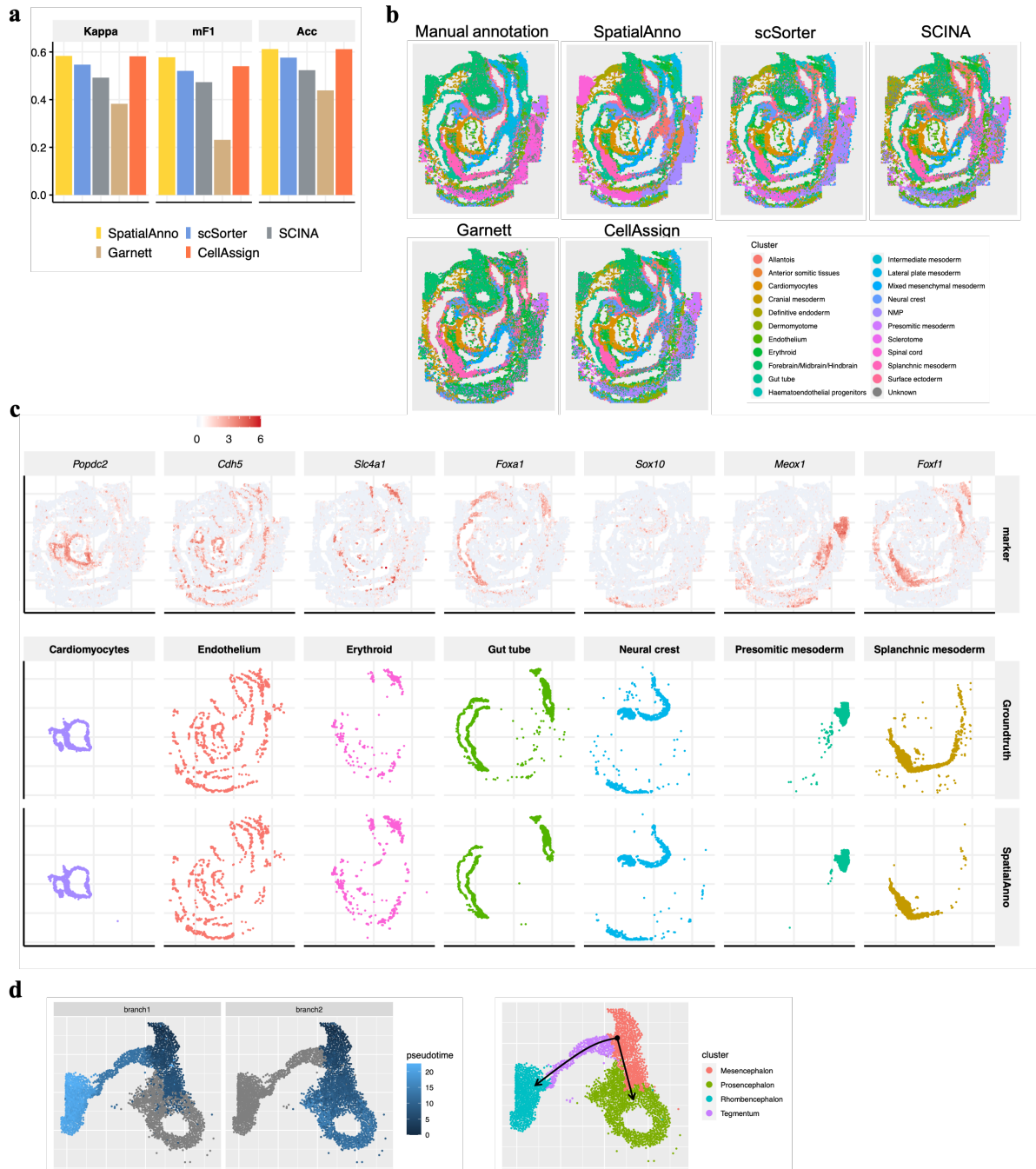


Figure 5: Spatial cell-type annotation of the mouse embryo dataset. **a** Bar plots of Kappa, mF1 and ACC showing the cell-type annotation accuracy of different methods. **b** Spatial annotations for ground truth, SpatialAnno, scSorter, SCINA, Garnett, and CellAssign. **c** Top, expression levels of corresponding cell-type-specific marker genes. Bottom, annotations of ground truth and SpatialAnno are shown on each spot. **d**, Left: latent time trajectory generated by slingshot on low dimensional embeddings of SpatialAnno. Right: clustering of the forebrain/midbrain/hindbrain cells into four spatially distinct clusters representing different regions of the developing brain.